Cerebral organoids at the air–liquid interface generate diverse nerve tracts with functional output

Stefano L. Giandomenico[1], Susanna B. Mierau[2], George M. Gibbons[3], Lea M. D. Wenger[3], Laura Masullo[1], Timothy Sit[2], Magdalena Sutcliffe[1], Jerome Boulanger[1], Marco Tripodi[1], Emmanuel Derivery[1], Ole Paulsen[2], András Lakatos[3,4] and Madeline A. Lancaster[1]*

Neural organoids have the potential to improve our understanding of human brain development and neurological disorders. However, it remains to be seen whether these tissues can model circuit formation with functional neuronal output. Here we have adapted air–liquid interface culture to cerebral organoids, leading to improved neuronal survival and axon outgrowth. The resulting thick axon tracts display various morphologies, including long-range projection within and away from the organoid, growth-cone turning, and decussation. Single-cell RNA sequencing reveals various cortical neuronal identities, and retrograde tracing demonstrates tract morphologies that match proper molecular identities. These cultures exhibit active neuronal networks, and subcortical projecting tracts can innervate mouse spinal cord explants and evoke contractions of adjacent muscle in a manner dependent on intact organoid-derived innervating tracts. Overall, these results reveal a remarkable self-organization of corticofugal and callosal tracts with a functional output, providing new opportunities to examine relevant aspects of human CNS development and disease.

Cerebral organoids[1] have been shown to model early brain development with remarkable fidelity. Recent advances in this field have demonstrated their capacity to model neurogenesis[1,2], neuronal migration and positioning[3,4], and even their response to sensory input[5]. However, later neuronal maturation is limited by insufficient oxygen and nutrient availability owing to the lack of a blood supply. Recent advances have been made to improve survival either by providing growth factors such as brain-derived neurotrophic factor[5] or by transplanting neural organoids into a rodent host to allow for vascularization[6]. Not only was transplantation shown to result in unprecedented survival of cells owing to effective blood perfusion, but cells within the organoid were demonstrated to exhibit neural connectivity with the host brain.

Such in vivo transplantations point to the possibility that cerebral organoids have the intrinsic potential to form functional connections, particularly if survival can be improved. However, this approach is tedious and requires specialist skills to perform and analyze transplants, making it difficult to perform more extensive characterization on multiple samples. Thus, a fully in vitro system that would improve nutrient supply and could be easily scaled up would be ideal for more extensive studies. Although in vitro vascularization of tissue-engineered constructs is a high priority in the bioengineering field, as of yet, this has not been successfully accomplished in a manner that maintains self-organization and tissue architecture.

In an effort to improve oxygen supply but retain the accessibility and scalability afforded in vitro, we tested an entirely different approach: application and adaptation of a classic method of organotypic slice culture[7] at the air–liquid interface. We show that air–liquid interface cerebral organoids (hereafter referred to as ALI-COs) exhibit greatly improved survival and morphology with extensive axon outgrowths reminiscent of nerve tracts. Live imaging reveals a variety of axon guidance behaviors mimicking the dynamics seen in vivo. Furthermore, single-cell RNA sequencing (scRNA-seq) reveals separate clusters of intracortical- and subcortical-projection identities and we show that these correspond to the tract morphologies observed. Finally, through electrophysiological and co-culture studies, we demonstrate functionality of these tracts, which are even capable of eliciting coordinated muscle contractions in co-cultured mouse spinal cord–muscle explants. This approach is likely to be a useful new tool, not only because of its ease, but also due to its utility in studying axon guidance, tract formation, and connectivity in a human system.

Results

Culture of cerebral organoids at the air–liquid interface leads to improved survival and maturation. After optimizing sectioning and culture conditions (Fig. 1a, Methods), we found that ALI-COs displayed overall improved morphology compared with whole organoids (Fig. 1b–e and Supplementary Fig. 1a) as well as increased numbers of cortical neuron populations, suggesting improved survival (Fig. 1f,g). TUNEL assay further confirmed a decrease in cell death in ALI-COs (Fig. 1h,i).

ALI-CO cultures could be maintained for many months and continued to display improved morphology and survival compared with whole organoids (Fig. 1j and Supplementary Fig. 1b). By contrast, whole organoids exhibited a loss of neurons and an accumulation of reactive astrocytes, particularly along the surface of the

[1]MRC Laboratory of Molecular Biology, Cambridge Biomedical Campus, Cambridge, UK. [2]Department of Physiology, Development and Neuroscience, University of Cambridge, Cambridge, UK. [3]John van Geest Centre for Brain Repair and Division of Stem Cell Neurobiology, Department of Clinical Neurosciences, University of Cambridge, Cambridge, UK. [4]Wellcome Trust–MRC Cambridge Stem Cell Institute, Cambridge Biomedical Campus, Cambridge, UK. *e-mail: mlancast@mrc-lmb.cam.ac.uk

organoid (Fig. 1k and Supplementary Fig. 1c), similar to previous observations[8]. Astrocytes in ALI-COs exhibited a healthier morphology with numerous fine processes. Even after one year, ALI-COs still exhibited abundant healthy neurons with numerous axons and dendritic processes (Fig. 1l).

To examine neuronal morphology in more detail, we performed sparse labeling with green fluorescent protein (GFP), which revealed aligned neurons of the cortical plate (Fig. 2a) that displayed mature morphologies (Fig. 2b) with complex dendrites and dendritic spines (Fig. 2c). Neuronal morphology continued to mature with one-year-old ALI-COs displaying highly complex dendritic architectures (Fig. 2d and Supplementary Fig. 2a). Staining for pre- and post-synaptic markers demonstrated synapses decorating the dendrites (Supplementary Fig. 2b). We also observed various interneuron types and the presence of GABAergic synapses (Supplementary Fig. 2c–e). This suggests the various cortical neuron and synapse types are present to allow for functional circuit formation. Indeed, ALI-COs stained positive for the marker of neuronal activity c-Fos (Supplementary Fig. 2f). Multi-electrode array recordings (Supplementary Fig. 2g) revealed the presence of spontaneous neural activity (Fig. 2e–g and Supplementary Fig. 2h), which was blocked by tetrodotoxin (TTX, Supplementary Fig. 2i–l). We also performed whole-cell patch-clamp recordings of individual neurons demonstrating the ability to fire trains of action potentials on positive current injection (Fig. 2h,i). These findings suggest the acquisition of mature neuronal morphology and establishment of activity in ALI-COs.

Long-term live imaging reveals axon outgrowth dynamics. Because the slice culture is easily tractable for live imaging, we examined axon guidance in GFP-labeled neurons over extended time periods (Fig. 3a and Supplementary Fig. 3a). Initial axon outgrowth was highly dynamic (Fig. 3b, Supplementary Fig. 3b and Supplementary Videos 1 and 2) whereas later axons projected in a directional fashion (Fig. 3c and Supplementary Video 3) and with greater velocity within bundles of axons (Fig. 3d, Supplementary

Fig. 3c and Supplementary Videos 4 and 5). These behaviors are reminiscent of the axon outgrowth dynamics of pioneer axons and follower axons of established tracts[9]. Indeed, ALI-COs displayed robust bundles of axons (Supplementary Fig. 3d) that became reinforced over time (Fig. 3e) rather than randomly filling with axons in all directions as is more typically seen in vitro[10]. Overall, the resultant axon bundles showed specific orientations and a high degree of coherency that is typical of tract morphology (Fig. 3f and Supplementary Fig. 3e).

Interestingly, these axon tracts could be observed to project within local regions, across the organoid over long distances, and even away from the organoid altogether (Supplementary Fig. 3f,g). Some tracts crossed in a manner similar to decussation (Supplementary Fig. 3h and Supplementary Video 6), with incoming growth cones retaining their directionality on arrival at the intersection, whereas other growth cones and tracts could be seen exhibiting turning behaviors (Supplementary Fig. 3c,i and Supplementary Video 7). Finally, axon bundles could be seen extending as a whole, with incoming growth cones projecting at a fast pace, whereas the tract-leading edge progressed much more slowly (Fig. 3g and Supplementary Video 8).

ALI-COs exhibit axon tracts with diverse morphologies and the presence of endogenous guidance molecules. Live imaging results point to the establishment of diverse axon tract morphologies; however, these visible tracts were only a subset of axons labeled by electroporation. To visualize the full diversity of axon tracts, we stained mature ALI-COs with SMI312, a broad marker of axons, which could be seen originating within discrete lobules and merging to form dense axon bundles (Fig. 4a) reminiscent of intracortical tracts of the CNS. To further investigate these internally projecting tracts, we performed staining for the specific marker of the developing corpus callosum, NRP1[11], which revealed a subset of ALI-CO tracts (Fig. 4b) that often appeared thicker and more fibrous than NRP1-negative tracts (Supplementary Fig. 4a). These tracts, like those observed by live imaging, could often be observed turning, suggesting the presence of endogenous attractants or repulsants that may

---

Fig. 1 | Culture at the air–liquid interface leads to improved neuronal survival and morphology. a, Schematic of the culture set-up as detailed in Methods. **b**, Immunohistochemistry for the marker SMI312 (red) to stain axons and MAP2 (green) for dendrites on representative sections of whole versus ALI cerebral organoid cultures. ALI-CO age is 82 d total (sliced at 61 d plus 21 d under ALI conditions). Whole organoid age is 90 d. Dashed line indicates the border of healthy neurons along the organoid surface. Inset shows a higher magnification of a lobule containing radially aligned neurons of the cortical plate (bracket), and arrows indicate SMI312 positive inward projecting tracts. **c**, Quantification of overall SMI312 levels reveals increased axon staining in ALI-COs. **P = 0.0022, two-tailed Mann–Whitney test, n = 6 whole organoids from two independent batches (ages: 90–105 d) and n = 6 ALI-COs from two independent batches (ages: 85–92 d); error bars are s.d. **d**, Whole organoids exhibit less-aligned axon staining as demonstrated by OrientationJ analysis (detailed in Methods) of SMI312 staining (Supplementary Fig. 1a), whereas axons in ALI-COs are more aligned. Pixel brightness corresponds to coherency of aligned structures and hue corresponds to energy, where pixels with higher energy report less isotropic and more oriented structures[23]. Images are representative of six samples from two independent batches each. **e**, The product of OrientationJ coherency and energy output levels was quantified in whole organoids compared with ALI-COs, demonstrating more aligned structures. **P = 0.0022, two-tailed Mann–Whitney test, n = 6 for each (same samples quantified as in **c**); error bars are s.d. **f**, Staining for deep-layer (CTIP2+) and upper-layer (CUX2+) neurons reveals increased numbers of both populations in ALI-COs with a particularly strong effect on deep-layer neurons, whereas most of the staining for CTIP2 is unspecific in whole organoids at this stage (age of whole organoids: 116 d, age of ALI-COs: 120 d, of which 36 d were under ALI conditions). **g**, ALI-COs display significantly higher numbers of CTIP2+ and CUX2+ neurons than whole organoids. Statistical analysis was carried out on a total of six whole organoids from three independent batches and six ALI-COs from two independent batches each with ages ranging between 98 and 105 d total in culture. *P = 0.0411, **P = 0.0022, two-tailed Mann–Whitney test; whiskers are minimum and maximum values, center line is median and limits are upper and lower quartiles. **h**, Representative TUNEL staining (red) in cryosections of whole organoids compared with ALI-COs used for quantifications in **i** reveals increased cell death in whole organoids. Inset is higher magnification of outlined region. **i**, Quantification of TUNEL+ cells in six whole organoids from three independent batches and six ALI-COs from two independent batches with ages ranging between 98 and 105 d total in culture shows that whole organoids display significantly higher levels of cell death compared with ALI-COs. **P = 0.0022, two-tailed Mann–Whitney test; error bars are s.d. **j**, Thirty-week-old whole organoid compared with age-matched ALI-CO (142 d ALI conditions, 210 d total) stained for axons (SMI312) and dendrites (MAP2) demonstrates continued survival and improved morphology in organoids kept under ALI conditions. Representative image of one of three ALI-COs stained compared with one whole organoid. **k**, Higher magnification of a 30-week-old whole organoid and an age-matched ALI-CO stained for glia (GFAP) and neurons (TUBB3), showing increased neurons and healthier astrocyte morphology in the ALI-CO. Representative image of one of three ALI-COs stained compared with one whole organoid. **l**, A 1-year-old ALI-CO (275 d under ALI conditions) stained for axons (SMI312) and dendrites (MAP2) continues to display abundant healthy neurons with evident axon tracts. Three ALI-COs from one organoid were stained with similar morphologies. Scale bars, 500 μm (**b**, **d**, **h**, **j** and **l**) and 100 μm (**f**, **k** and **l** inset).

guide axon outgrowth during the establishment of ALI-CO tracts. To test this hypothesis, we performed staining for known guidance cues including WNT5A, Netrin, and EphrinB1[12]. We observed striking foci of WNT5A near to, and surrounding, NRP1^{+} tracts (Fig. 4c) similar to the pattern described at the glial wedge in vivo that helps guide callosal tracts[13]. Furthermore, we also observed a subset of NRP1^{+} tracts that were also positive for the WNT receptor RYK (Supplementary Fig. 4b)[14], as well as internally projecting tracts positive for EphrinB1 (Supplementary Fig. 4c). Finally, staining for the attractant Netrin-1 revealed large foci with numerous nearby inwardly projecting tracts oriented toward the Netrin-1 signal (Fig. 4d).
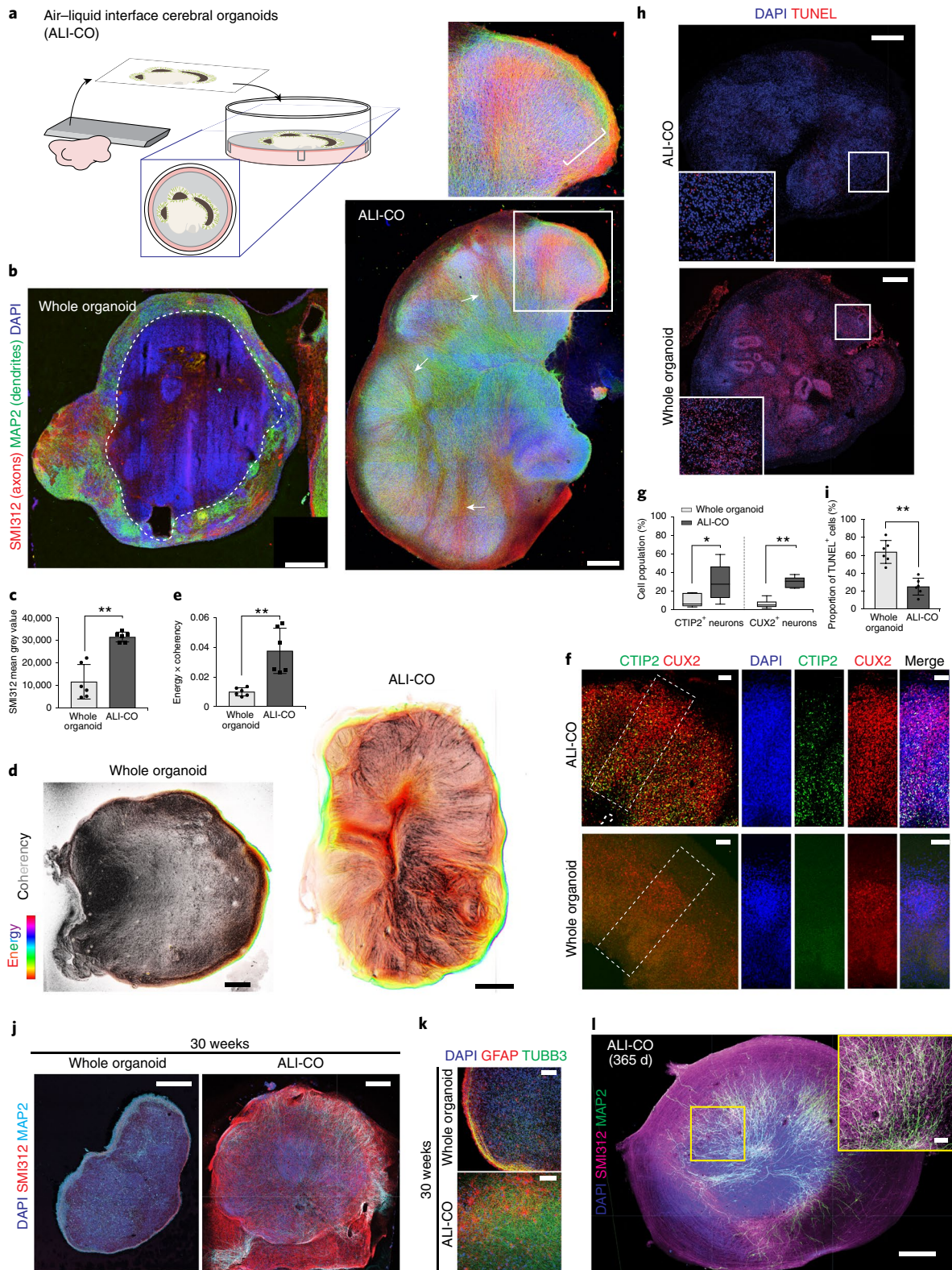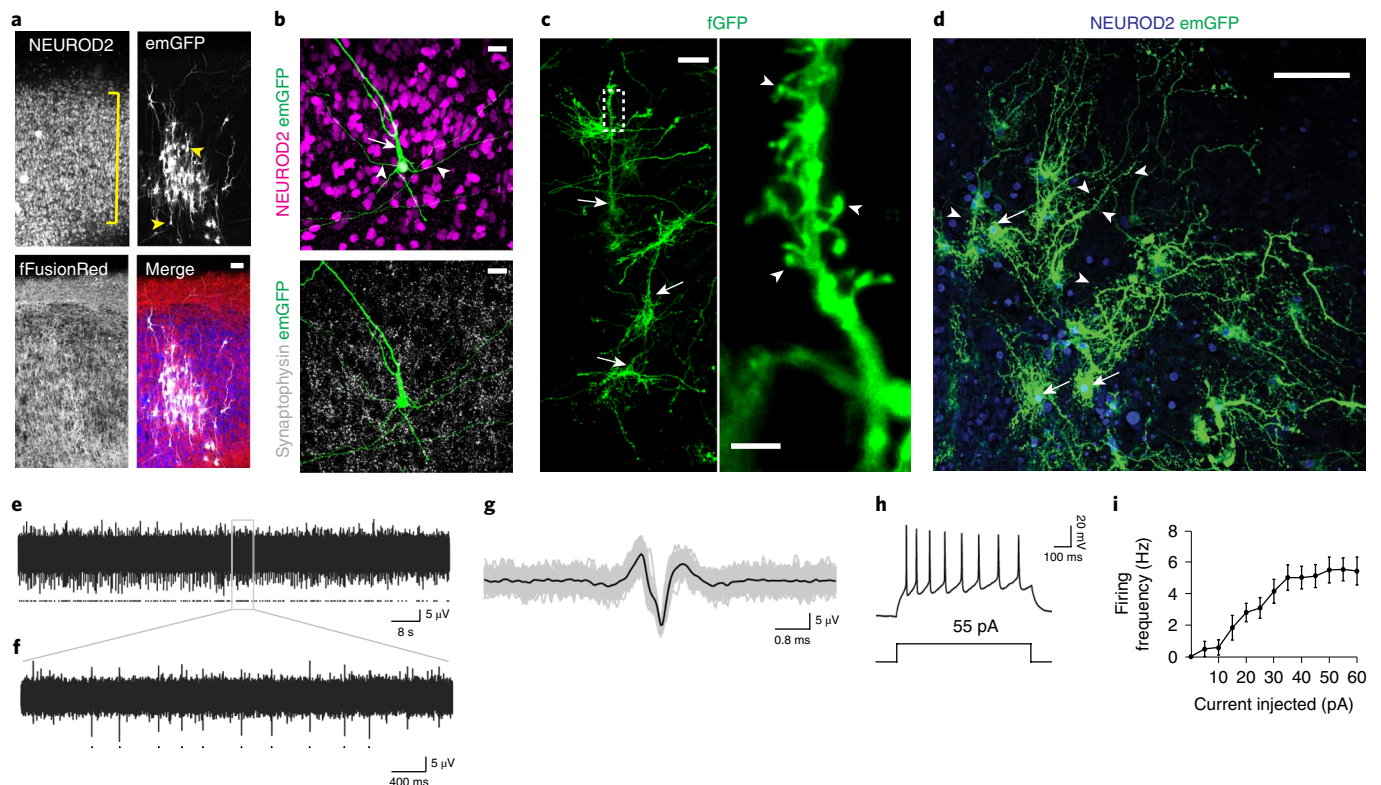
Fig. 2 | ALI-CO cultures exhibit mature neuronal morphology and function. a, Sparse labeling in an ALI-CO after 37 d under ALI conditions (80 d total) by Sendai-virus encoding emGFP (white) reveals radially aligned neurons (NEUROD2, blue) with complex dendritic architectures and pyramidal morphologies (arrowheads) within the aligned cortical plate (bracket). All cells contain fFusionRed (red) to visualize the overall tissue morphology. **b**, Higher magnification of a maximum-intensity projection of a single emGFP (green) labeled neuron (NEUROD2^{+}, magenta) displaying typical pyramidal morphology with primary dendrite (arrow) and basal dendrites (arrowheads). Synaptophysin (white) reveals extensive synaptic staining throughout. **c**, Electroporation of membrane targeted farnesylated GFP (fGFP, green) reveals complex dendritic architecture of radially aligned pyramidal neurons (arrows) in a maximum-intensity projection with evident dendritic spines (arrowheads, inset) in an ALI-CO after 51 d under ALI conditions (143 d total) **d**, Sparse labeling of a 1-year-old ALI-CO (90 d plus 275 d under ALI conditions) with Sendai-virus encoding emGFP labels several individual neurons (arrows) with highly complex dendritic architectures and abundant dendritic spines (arrowheads). Sparse labeling with emGFP and fGFP in **a**–**d** was performed on three ALI-COs from three organoids with similar results. **e**, Two minutes (2 min) of spontaneous activity recorded from a single electrode of a MEA in an ALI-CO after 54 d under ALI conditions (117 d total); detected action potentials marked with dots. **f**, A 5-s segment from the recording shown in **e** (expanded from gray box). **g**, Overlay of all detected spikes (gray, marked by dots in **f**) with mean waveform in black. **h**, Whole-cell patch-clamp recordings of action potentials evoked by a 55 pA current injection. **i**, Frequency–current (F–I) curve showing average action potential firing rate with increasing amplitude of current injection (error bars are s.e.m., $n = 13$ cells from seven ALI-COs of three independent organoid batches). Scale bars, 50 µm (**a**, **c**), 20 µm (**b**), 5 µm (**c** inset) and 100 µm (**d**).

In addition to internally projecting tracts, we observed outgrowth of axon tracts projecting away from the organoid altogether (Fig. 4e and Supplementary Fig. 4d). Retrograde tracing with the lipophilic dye DiI (Supplementary Fig. 4b), as well as tract coherency/alignment analysis (Fig. 4f), revealed the morphology of these escaping tracts as well as the location of the responsible projection neurons (Supplementary Fig. 4e). These 'escaping' tracts appeared most similar to subcortical projections.

scRNA-seq reveals the full repertoire of cortical neuron types. The presence of a variety of axon tract morphologies suggests that ALI-COs might display various neuron identities that could exhibit different projection behaviors. To test this possibility, we performed scRNA-seq on ALI-COs to examine the full repertoire of cell types. We analyzed six slices from three ALI-CO preparations with an average of 4,427 cells per sample, which were processed through the 10× single-cell genomics platform (Methods). Unbiased clustering of cell populations was achieved by principal component analysis using highly variable genes as input and was visualized following dimensionality reduction using t-distributed stochastic neighbor

embedding (tSNE) (Fig. 5a). This resulted in the separation of six well-defined major clusters (C1–C6, Fig. 5b).

Gene Ontology (GO)-term analysis (false-discovery rate (FDR) > 0.1% with highest fold-enrichment) of the top 50 differentially expressed genes (Fig. 5c) raised a possibility that developmental cell states define the main cell populations, reflecting stages of in vivo cortical development (Fig. 5d). In support of this, pseudotime analyses (Supplementary Fig. 5a,b) and gene expression correlation (Supplementary Fig. 5c–e) revealed a similar co-expression pattern of progenitor zone and neuronal-layer marker genes in the organoids to that shown for the age-matched fetal brain. Thus, we next compared the average expression of developing cortical cell-type-, cell-state-, and region-specific marker genes (Methods). Cluster identities better corresponded with cell-types and maturity (Fig. 5e) than brain region specific markers (Supplementary Fig. 5f,g). This also supports previous findings that the enCOR method used as the starting material for ALI-COs preferentially generates a forebrain identity[4].

Cell-type and maturity markers revealed a distinct population of deep-layer subcortical projection neurons (C1, for example, CTIP2, FEZF2), upper layer intracortical (callosal) projection neurons and
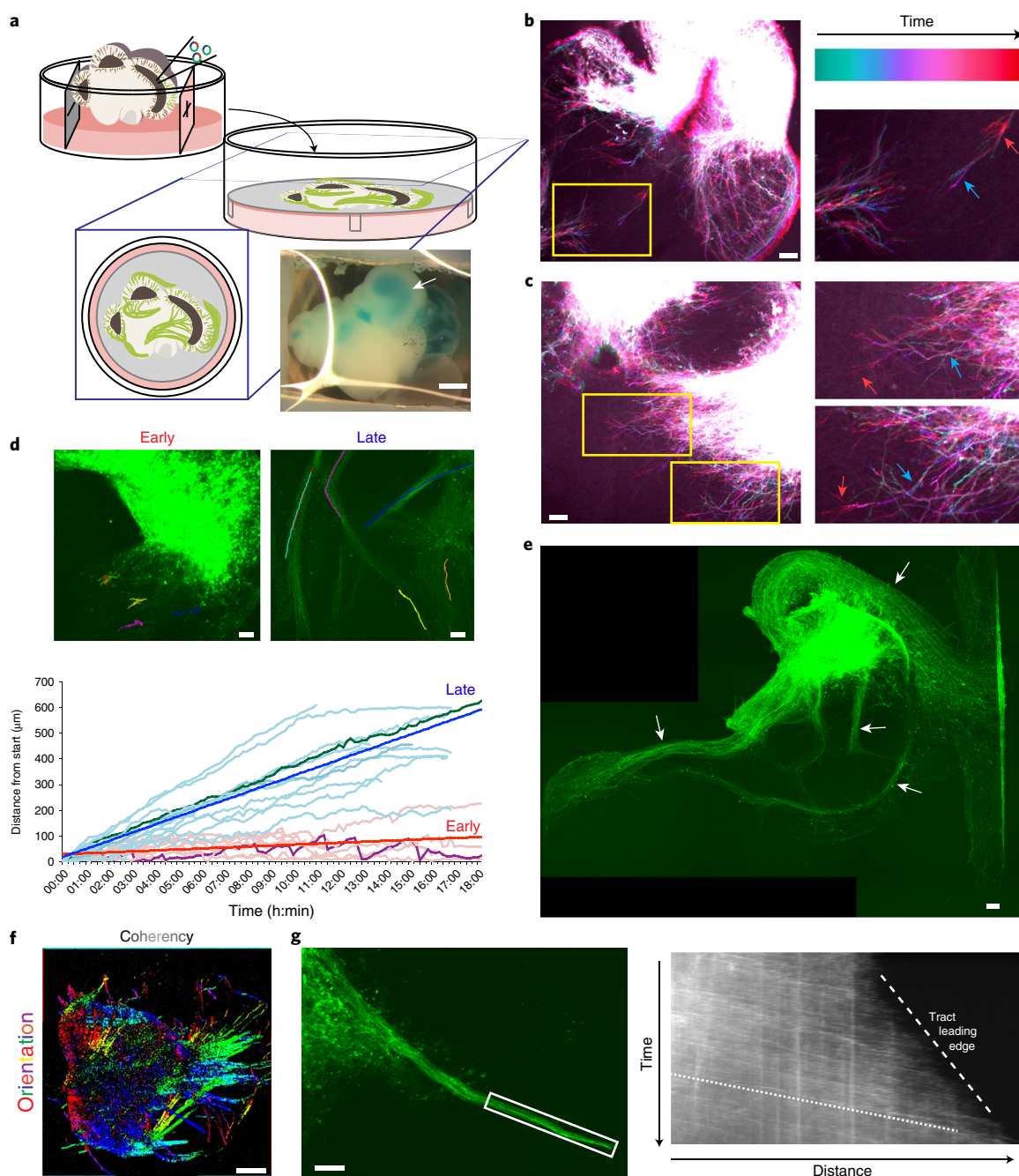
Fig. 3 | Neurons of ALI-COs exhibit dynamic axon guidance behaviors. a, Schematic of electroporation and preparation of ALI-COs for live imaging. Inset image shows an organoid after plasmid injection along with a blue dye (FastGreen) to visualize the injected ventricle (arrow). **b**, Temporal projection image pseudocolored by time (Supplementary Video 2) of an electroporated ALI-CO after 5 d under ALI conditions (69 d total age) showing dynamic axon outgrowth with growth-cone retraction (blue arrow to red arrow in the higher magnification inset). Image is representative of five similarly staged and live-imaged ALI-COs. **c**, Temporal projection image (Supplementary Video 3) after 9 d at the ALI (73 d total age) showing more directed axon outgrowth with progressive extension (blue arrow to red arrow in higher magnification insets). Image is representative of three similarly staged and live-imaged ALI-COs. **d**, Tracing of individual growth cones over time from ALI-COs under ALI conditions for 2–5 d (early) and 14–24 d (late) reveals disparate behaviors and velocities (see Supplementary Videos 1 and 4). Growth cones in later, established tracts exhibit a higher velocity (bold blue and red lines are average linear regression for each dataset), whereas earlier growth cones exhibit dynamic retractions (visible in a highlighted trace in purple compared with later highlighted in green). An example image of each is shown above with superimposed traces. Tracing was done on 9 growth cones (early) and 12 growth cones (late) from 4 organoids generated from 2 independent batches. **e**, Axon tracts after 18 d ALI culture (88 d total) demonstrating numerous dense bundles (arrows) with a non-random projection pattern. Note the same overall pattern but with reinforced bundles compared with Supplementary Fig. 3d, which was taken 4 d earlier. Shown is one representative ALI-CO of seven similarly staged and imaged ALI-COs. **f**, Directional image analysis for the orientation (hue) and coherency (brightness) of aligned axon tracts (original image is shown in Supplementary Fig. 3e). The image is representative of five such directional analyses performed with similar results. **g**, Still image (left) and kymograph (right) of an extending tract (boxed region) (Supplementary Video 8). Note the higher velocity (shallow slope, dotted line) of incoming growth cones, whereas the leading edge of the tract as a whole progresses more slowly (steep slope, dashed line). Representative results of three experiments performed. Scale bars, 1mm (**a**), 100 μm (**b**–**e**, **g**) and 500 μm (**f**).
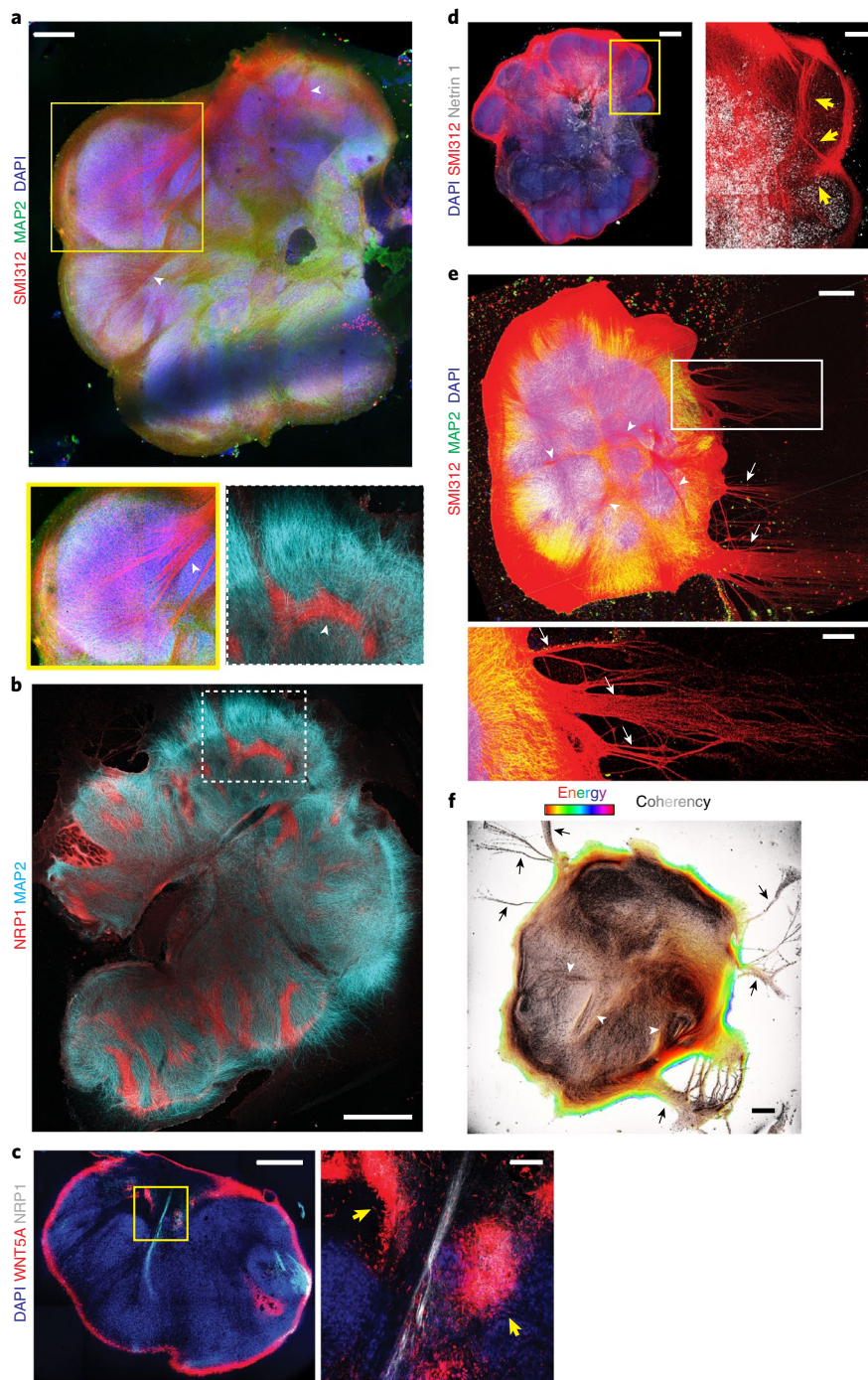
Fig. 4 | ALI-COs exhibit diverse axon tract morphologies. a, Staining for all axons (SMI312) and dendrites (MAP2) on an ALI-CO after 36 d under ALI conditions (85 d total) reveals thick bundles (arrowheads) that can be seen projecting within the organoid and merging to form large tracts (inset below, arrowhead). Image is representative image of seven ALI-COs stained with similar results. **b**, Staining of ALI-COs after 49 d under ALI conditions (120 d total age) for the corpus callosum marker NRP1 reveals several internal tracts that are positive and even appear to turn. MAP2 stains dendrites. The image is representative of four ALI-COs stained with similar results. **c**, Left: co-staining for NRP1 and the callosal guidance factor WNT5A reveals discrete foci (yellow arrows) surrounding an NRP1$^+$ internally projecting tract in an ALI-CO after 54 d under ALI conditions (117 d total). Right: magnification of boxed region. Representative image of two ALI-COs stained with similar results. **d**, Staining of ALI-COs after 32 d under ALI conditions (81 d total age) for the axon attractant Netrin 1 reveals large areas of positivity with evident tracts (SMI312$^+$, arrows) projecting inward and toward the Netrin 1 signal. The image is representative of two ALI-COs stained with similar results. **e**, Axon (SMI312) and dendrite (MAP2) staining of an ALI-CO with tracts 'escaping' from the main mass (arrows) after 34 d under ALI conditions (89 d total), in addition to internal projections (arrowheads). The image is representative of seven ALI-COs stained with similar results. **f**, Analysis of axon alignment and coherency by OrientationJ analysis (Methods) of SMI312 staining in a whole ALI-CO after 41 d under ALI conditions (89 d total). Pixel brightness corresponds to coherency and hue corresponds to energy, where pixels with higher energy report less isotropic and more oriented structures[23]. Analysis shown is representative of six ALI-COs with similar results. Scale bars, 500 μm (**a**, **c**–**f**), 1 mm (**b**), 100 μm (**c** inset) and 200 μm (**d** inset and **e** inset).
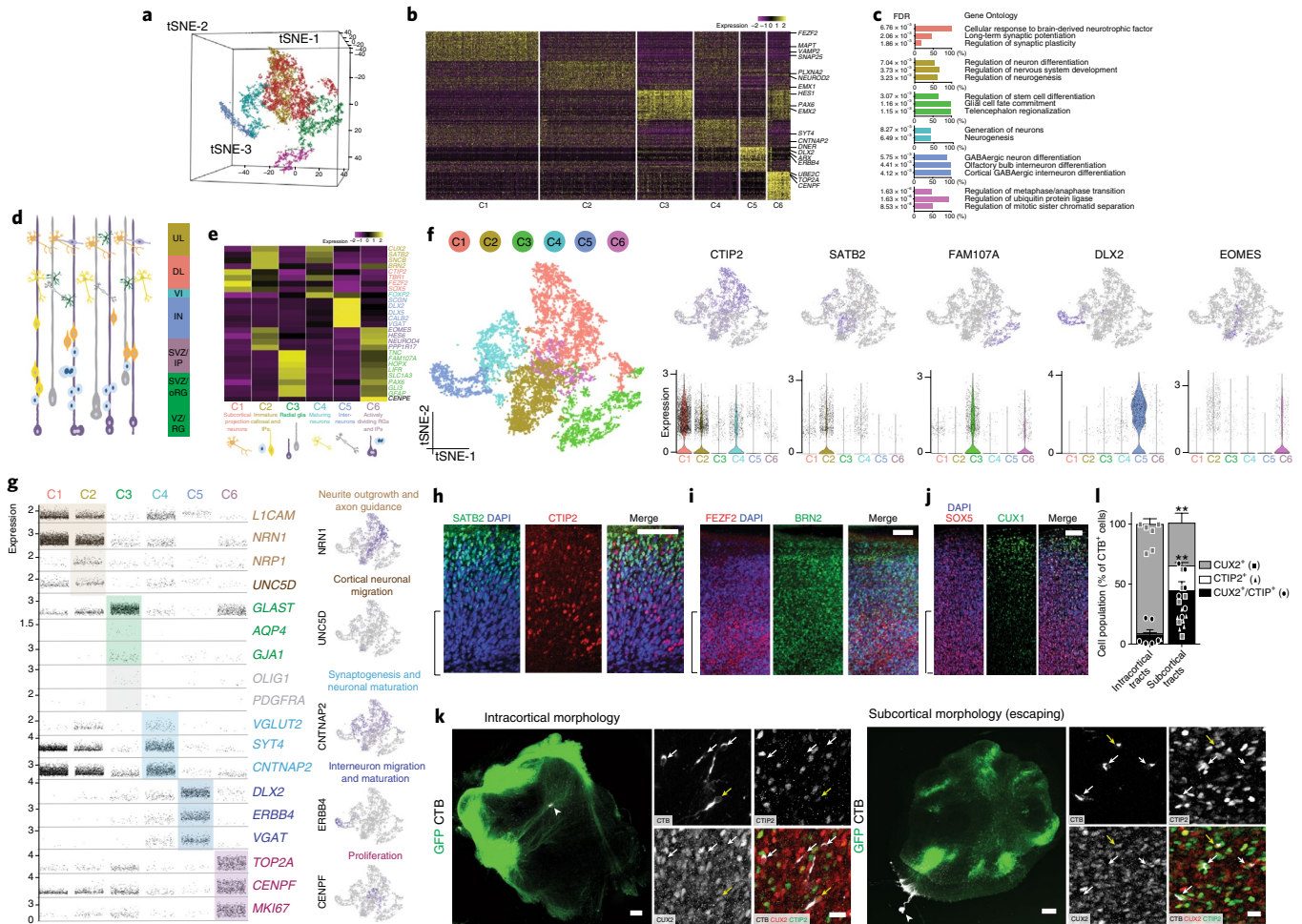
Fig. 5 | ALI-COs contain diverse neuron identities that exhibit specific projection patterns. a, Unbiased tSNE separation of clusters based on scRNA-seq data of 13,280 cells from six ALI-COs of three organoids (sample and data acquisition detailed in Methods) visualized in a 3D space, showing six main populations. **b**, Heat map demonstrating scaled levels of the top-50 differentially expressed genes in the main clusters (C1–C6) with example genes (shown at right). **c**, Histograms of the three top GO biological-process annotations that were defined on the basis of the highest fold-enrichment amongst the most significant terms (Fisher's exact test with FDR multiple test correction above 0.1% by http://geneontology.org, $P < 0.001$, $n = 50$ top differentially expressed genes per cluster). Color coding of bars represent cluster identities. **d**, Schematic of cells residing in the different layers of the fetal human cortex: ventricular zone (VZ) containing radial glia (RG), subventricular zone (SVZ) containing outer/basal radial glia (oRG) and intermediate progenitors (IP), deep (DL) and upper cortical-plate layers (UL), as well as interneurons (IN) and layer 6 neurons (VI). **e**, Heat map showing the scaled mean expression levels of layer- and cell-type-specific genes within the six unbiased clusters, identifying the major cell populations. The color coding of layers, marker genes (right side) and cell types (bottom) corresponds with cluster identities (C1–C6, bottom). **f**, Two-dimensional tSNE plots of clusters (left) and the distribution of cells expressing layer or cell-type marker genes across the main populations (right top). Scatter plots show the distribution of corresponding normalized gene expression values per cell within each cluster (right bottom); the violin plots overlaid on the scatter plots are displayed where the proportion of cells expressing a given gene is the highest. Tails of the plot have been trimmed to represent the maximum and minimum values of expression levels. The central hinge represents the median value for each cluster. The distribution in each cluster is based on the filtered and merged datasets derived from the six organoid slice samples ($n = 4{,}191$ cells for C1; 3,565 cells for C2; 2,068 cells for C3; 1,658 cells for C4; 952 cells for C5; 846 cells for C6). **g**, Left: scatter plots demonstrating the normalized gene expression levels of genes per cell across the six main clusters with a focus on relevant neuronal, progenitor and glial functions. Right: feature plots demonstrate example genes expressed by populations confined to a particular cluster or by multiple cell populations. Color coding represents functional gene associations. **h**, Staining of ALI-COs after 20 d under ALI conditions (90 d total age) for SATB2 reveals the presence of this upper-layer marker and its distribution in a more superficial region, compared with CTIP2. **i**, FEZF2+ deep-layer cells and BRN2+ superficial-layer cells are also present and exhibit appropriate distributions in an ALI-CO generated from another organoid after 20 d under ALI conditions (90 d total age). **j**, Superficial CUX1+ cells are present in more superficial regions, with SOX5+ cells in deeper locations, in ALI-COs after 20 d under ALI conditions (84 d total age). Brackets in **h**–**j** denote the deeper regions of the ALI-CO cortical plate. **h**–**j**, Images are representative of a region of a single ALI-CO stained for each. **k**, Representative images of samples used for retrograde labeling by CTB microinjection (arrowheads indicate injection site) and quantification in **l** reveal disparate identities contributing to distinct tract morphologies. Inset images are maximum-intensity projections of Z-stacks used for quantifications. Individual channels and merge are shown. Yellow arrows indicate CTIP2+/CUX2+ cells and white arrows indicate CUX2-single-positive (intracortical morphology, left) or CTIP2-single-positive (subcortical escaping morphology, right) cells. **l**, Quantification of CTB+ cells indicate that tracts with internal projection morphology (left) traced back primarily to CUX2+ callosal projection identity cells, while escaping subcortical morphology tracts traced back primarily to CTIP2+ identity cells, as well as CTIP2+/CUX2+ cells. Six ALI-COs for each condition (intracortical and escaping) from four different organoids were labeled, and all CTB-labeled cells across the entire depth of antibody penetration in whole ALI-CO slices were counted for CUX2 or CTIP2 staining. Statistics were performed only on comparisons of single-positive cells because double-positive cells are of indeterminate identity. **$P = 0.0022$, two-tailed Mann–Whitney test, $n = 6$; error bars are s.e.m. ALI-COs stained after 33 d under ALI conditions (97 d total age). Scale bars, 100 μm (**h**–**j**), 300 μm (**k**) and 20 μm (**k** inset).

intermediate progenitors (C2, for example, SATB2, EOMES), ventricular and subventricular zone radial glial cells (C3, for example, GFAP, FAM107A), more mature upper- and deep-layer neurons (C4, for example, FOXP2, CUX2), interneurons (C5, for example, DLX2) and actively dividing cells with intermediate progenitor and radial glia markers (C6, for example, CENPE, EOMES, GLAST) (Fig. 5d–f). Staining for upper-layer and deep-layer identities further supported the presence of a variety of projection types (Fig. 5h–j). Interestingly, the overlapping cluster of upper-layer neurons and intermediate progenitors suggests many of the upper-layer neurons may still be quite immature, which would match previous findings that upper-layer neurons are actively being generated at this time point (69–75 days) in organoid development[8].

We then examined if the cluster-forming cell types were associated with a gene-expression profile that appropriately corresponds with their expected functional characteristics, such as axon projection and neuronal-circuit formation. Many of these were also present within the differentially expressed genes (Fig. 5g). Genes associated with axon outgrowth/tract formation (L1CAM, NRN1) were expressed more abundantly and at increased levels in the C1–C2 clusters formed by extra- and intracerebral-projection neurons and to a lesser extent in the C4 population. The C4 cluster showed higher levels of more mature markers of excitatory and inhibitory synapse formation (VGLUT2, CNTNAP2, SYT4). The high relative expression of DLX2, DLX5, ERBB4 and VGAT in C5 further indicated a very distinct interneuron population and, together with histological data (Supplementary Fig. 2c–e), raised a possibility for the presence of early cortical circuits. Some cells with functionally relevant markers of astroglial maturity (AQP4, GJA1) and the

oligodendrocyte lineage (OLIG1, PDGFRA) were present in C3, but to a very low degree at this relatively early stage. The C6 progenitor population displayed high levels of transcripts indicative of cell proliferation (CENPF, TOP2A), corresponding with the amplifying cortex-forming populations. Overall there was a well-defined association between celltypes and their expected function suggested by the molecular profiles in each cluster (Fig. 5f,g).

To test whether, as seen in vivo, the upper- and deep-layer neuron populations in ALI-COs project as tracts with distinct morphology, retrograde labeling with cholera-toxin subunit B (CTB) was performed on escaping and internal axonal bundles with immunohistochemistry for both CTIP2, marking subcortical projecting identities, and CUX2, marking callosal projecting identities (Fig. 5k,l). Whilst $91.1 \pm 11.0\%$ (mean ± s.d.) of neurons projecting into internal tracts stained specifically for the callosal marker CUX2, only $35.7 \pm 19.9\%$ of escaping tracts were positive for only this marker. Instead, $65.4 \pm 24.3\%$ of escaping-tract-projection neurons were CTIP2+ with $20.6 \pm 6.4\%$ being specifically stained for only this marker, compared with $1.1 \pm 1.5\%$ of internal-projecting neurons. These data suggest the morphology of the tracts matches the correct molecular identity.

ALI-COs exhibit neural networks with functional output. We sought to test the functionality of these tracts, focusing first on the internal-projecting tracts. We employed three-dimensional (3D) multi-electrode arrays (MEAs) to perform extracellular recordings (Fig. 6a) and infer the functional connectivity within ALI-COs from analysis of correlated spontaneous activity[15]. ALI-COs showed network bursts (Fig. 6b and Supplementary Fig. 6a,b) in

Fig. 6 | Functional connectivity in intracortical and subcortical projecting axon tracts. a, Image of a 130-d-old ALI-CO (39 d under ALI conditions) on transfer to the 3D multielectrode array. **b**, Traces of spontaneous activity (3.4 ms long) in the 59 recording electrodes at the time of a network burst. Reference electrode location and trace are indicated by arrows in **a** and **b**. **c**, Network plot showing functional connectivity between specific sites within the ALI-CO shown in **a**. Line thickness represents strength of correlation in the spontaneous activity recorded between connected nodes (59 recording electrodes of the MEA) in the network, and size of the node indicates the number of connections. Correlated activity was determined using the spike-time tiling coefficient as detailed in Methods. **d**, Distribution of distances between functionally connected nodes in **c** shows short-, medium- and long-range connections within the ALI-CO. The peak of highest correlated connection distances occurs at approximately 400 μm, the peak of the moderately correlated connection occurs at approximately 600 μm, and the lowest correlated connection occurs at approximately 800 μm. **e**, Schematic of the ALI-CO–mouse spinal cord co-culture with a representative image (right) taken just after sectioning (after 62 d of organoid culture). **f**, Example of innervation of mouse spinal cord by tracts derived from human ALI-COs 68 d after the initiation of co-culture (123 d total organoid age). Left: brightfield image shows overall positioning of the tissues, with evident axon tracts (arrows) projecting from the ALI-CO (bottom right) to the mouse spinal cord (top left). Right: staining with the human-specific marker STEM121 reveals that these are ALI-CO-derived, and MAP2 staining reveals mouse neurons within the spinal cord and also stains neurons of the human tissue, which is double-positive. Images in **e** and **f** are representative of six co-culture experiments performed. **g**, Immunofluorescence using a human-specific antibody against the presynaptic marker synaptophysin (SYP), STEM121, MAP2 and the postsynaptic marker Psd95 and high magnification imaging in the mouse spinal cord region of a mouse spinal cord–ALI-CO co-culture after 32 d (84 d total organoid age) reveals mature human–mouse synapses with human SYP juxtaposed to Psd95 along the surface of mouse Map2+ and STEM121+ neurons. Lower magnification image is a maximum-intensity projection. Staining was performed on one sample of six co-culture experiments. **h**, Brightfield images of 32-d-old (84 d total organoid age) human–mouse co-culture used for **i–l**. Images show pre- (outlined in blue) and postaxotomy (outlined in red) with a stimulation electrode (yellow dashed outline) placed on axon tracts leading from the organoid. Yellow box, region imaged for muscle contraction traces in **i–l**; white dashed box, region shown in Supplementary Fig. 6g; red dashed line, site of axotomy. Image is representative of six co-culture experiments used for stimulation experiments as shown in **i–l**, two of which included axotomy as shown, with similar results in all. **i**, Spontaneous muscle contractions recorded as displacement (Methods) of the co-culture shown in **h**. Recording was made before stimulation of the tissue. **j**, Muscle displacement (contraction) amplitude in response to increasing amplitude of single current pulses (black arrows, 2 mA to 20 mA, 120 μs long) at 30, 40, 50 and 60 s of the recording (Supplementary Video 11). **k**, Evoked muscle contractions (Supplementary Video 12) pre- (blue) and postaxotomy (red) in response to single current pulses (black arrows, 15 mA, 120 μs long) applied at 30, 60, 75, 90, 105, 120, 135 s during the recording (150 s total duration). **l**, Evoked muscle contractions (Supplementary Video 13) pre- (blue) and postaxotomy (red) in response to 30 s of 1 Hz TTL stimulation with 15 mA current pulses (black hash marks indicate the 120 μs time window of stimulation). Both spontaneous and evoked contractions were abolished by axotomy (Supplementary Video 14) in **k** and **l**, whereas only a few very low amplitude contractions are seen. **m**, Overlay of evoked muscle contraction waveforms elicited by repeated current pulses (15 mA, 160 μs long, 0.6 Hz), and waveform average (black), showing the first peak at approximately 37 ms after stimulation. Reported above is a box and whisker plot capturing the spread of the individual contraction events ($n = 35$ contraction events; center line is median, limits are quartiles, whiskers are minimum and maximum). Red cross is an outlier with another outlier recorded at 1 s (not shown). Organoid recorded after 42 d under ALI condition (104 d total age). **n**, Evoked muscle contractions to 30 s of repeated current pulses (blue trace, 0.4 Hz, 25 mA, 180 μs long, time window of stimulation indicated by black hash marks) in a 21-d-old human–mouse co-culture (89 d total organoid age) (Supplementary Fig. 6j) were abolished by application of 2 μM TTX (orange trace) and restored (green trace) following wash-out with warm media (8×) and 30 min incubation at 37 °C. Scale bars, 1 mm (**a**), 500 μm (**e**, **h**), 200 μm (**f**), 5 μm (**g**) and 1 μm (**g** inset).

which neurons near multiple electrodes across the MEA showed simultaneous bursts of action potentials, as seen in mature neuronal networks[16]. Comparison of the correlated activity revealed densely connected local networks (Fig. 6c and Supplementary Fig. 6c) in which the highly correlated neuronal activity could be found within both short- and long-range connections between nodes (Fig. 6d). Interestingly, although the connections appeared stronger over shorter distances, the highest correlated activity occurred at a greater distance than the distance between two electrodes (which are 200 μm apart) suggesting these are not simply nearest-neighbor connections but that there is a degree of spatial specificity in the connections made. Overall, these findings point to specific spatial patterns of connectivity within ALI-CO cultures.

We next examined the functionality of the escaping, subcortical projecting tracts. ALI-COs were co-cultured with sections of the spinal column dissected from embryonic mice in which the associated peripheral nerves and paraspinal muscles were still intact[17] (Fig. 6e). After 2–3 weeks in co-culture, dense axon tracts from the ALI-COs could be seen innervating the mouse spinal cord (Fig. 6f) and synapses were visible between human projecting axons and neurons of the mouse spinal cord (Fig. 6g). Live imaging of the mouse muscle tissue revealed sporadic concerted muscle contractions with an irregular periodicity (Fig. 6h,i, Supplementary Fig. 6d and Supplementary Video 9). Importantly, these muscle contractions were coordinated and had high amplitude compared with the spontaneous uncoordinated twitches of individual muscle units
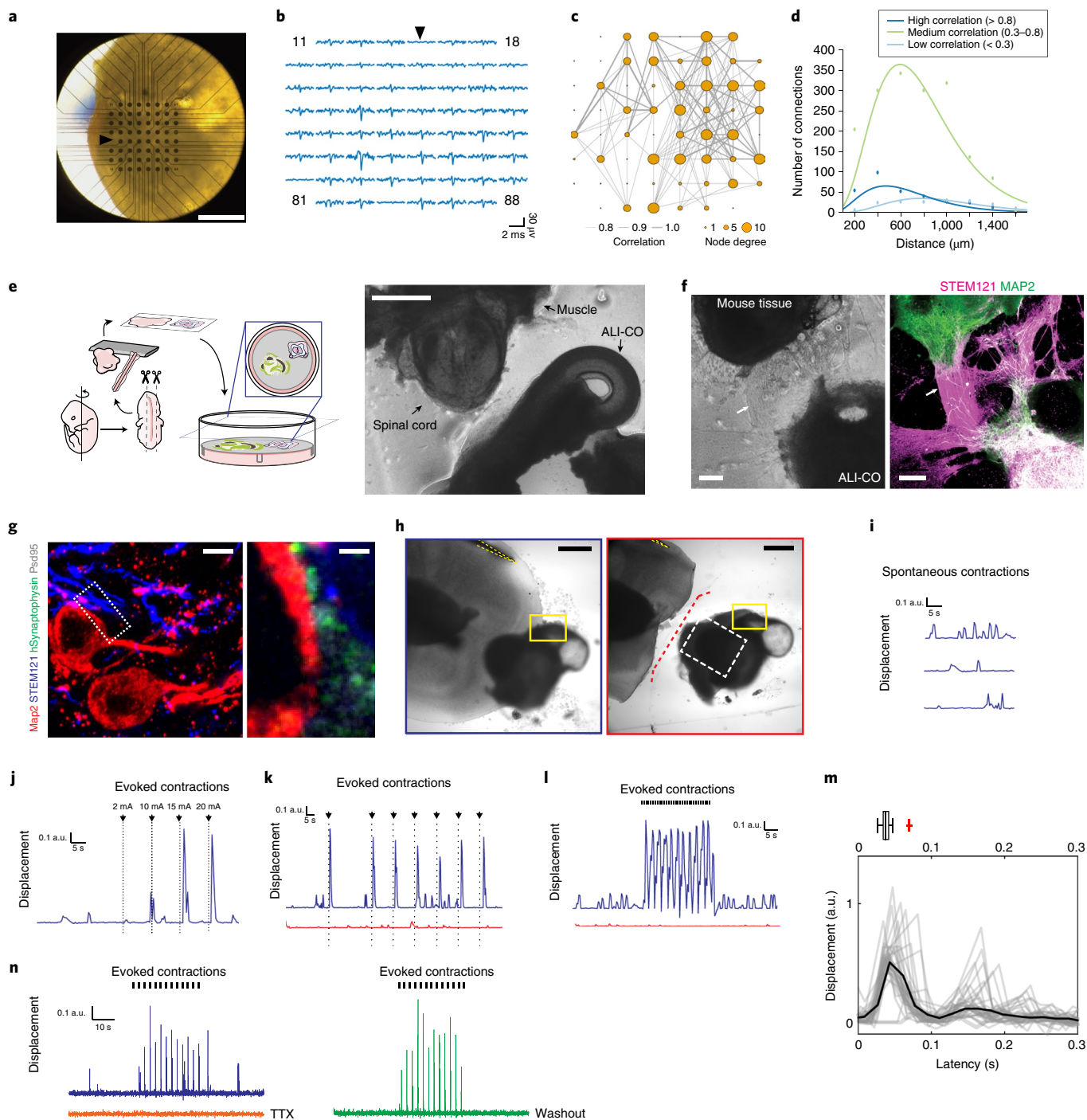
that could be observed in the absence of innervation by human tracts (Supplementary Fig. 6e). In addition, the coordinated, high-amplitude contractions of ALI-CO-innervated mouse tissue could be abolished by lesion of the ALI-CO axonal tracts, being replaced with low amplitude single-muscle-unit fibrillations (Supplementary Fig. 6d and Supplementary Video 10), pointing to specificity and dependence on ALI-CO tract innervation.

To test whether ALI-CO subcortical axon tracts could control the mouse paraspinal muscle contractions, we performed extracellular stimulation of the ALI-CO axon tracts and observed muscle response. A single brief stimulation of sufficient intensity of the axon tract could elicit a robust muscle contraction (Fig. 6j,k and Supplementary Fig. 6f). Evoked muscle contractions were intensity dependent such that larger stimulation currents increased the amplitude of the muscle contraction (Fig. 6j, Supplementary Fig. 6f and Supplementary Video 11), and we could reliably drive the muscle contractions with repeated stimulation (Fig. 6k and Supplementary Video 12), and at frequencies up to 1 Hz (Fig. 6l, Supplementary Fig. 6f and Supplementary Video 13). The median latency of response from stimulation to beginning of muscle contraction was approximately 37 ms (with a measurement uncertainty of 17 ms, the time interval between consecutive imaging frames) (Fig. 6m), which was remarkably similar to recorded latencies of the developing human descending motor pathway[18], and is also consistent with a polysynaptic circuit. The latency also suggests electrical stimulation was not activating the muscle directly but relied on the organoid neural tract. Indeed, staining of the responding tissues revealed bundles projecting into the mouse spinal cord (Supplementary Fig. 6g,h), and lesion of this tract eliminated the ability to evoke muscle contractions (Fig. 6h,k,l, Supplementary Fig. 6i and Supplementary Video 14). Finally, application of TTX to an intact ALI-CO–mouse spinal co-culture prevented evoked muscle contractions, which were restored after TTX washout (Fig. 6n and Supplementary Fig. 6j). These findings provide evidence that ALI-CO tracts can produce functional output to an external target.

Discussion

We find that by culturing cerebral organoids at the ALI, the tissue remains healthy over a very long period of time (we have tested up to one year). Importantly, we performed sectioning of organoids after the establishment of the cortical plate as described previously[4], thus first allowing proper tissue morphogenesis before ALI culture. In this way, the method is highly similar to slice culture typically performed on mid-neurogenesis-stage fetal cortex[19]. The axon dynamics observed in ALI-COs is quite striking, and patterns that ensue suggest a high degree of intrinsic organization. The bundling behavior further suggests proper tract formation, but importantly, it is distinct from the fasciculation previously seen in vitro, where bundles form indiscriminately between all neighboring clusters of neurons[20]. Furthermore, the presence of endogenous axon guidance cues along with turning behaviors points to similarities to in vivo development and supports the utility of ALI-COs for future studies of axon guidance through application of exogenous signals. Finally, studies with MEAs and explant co-culture point to functional connectivity within and between ALI-COs and external targets. We further show that tractotomy demonstrates specificity and can be used to study the effects of lesion.

These experiments show a functional output from a neural organoid. This allows study of neural connectivity on a complete circuit, with both input and output, making it possible to examine various aspects of how neurons connect, circuit rewiring, and even more complex aspects of neuronal processing. Furthermore, the ALI-CO approach could be used to model human conditions affecting connectivity. For instance, it opens the door to the study of neurodevelopmental conditions of the corpus callosum, neuronal circuit imbalances seen in epilepsy, and other defects where

connectivity is thought to play a role, such as in autism and schizophrenia. Finally, brain organoids are increasingly being used to study degenerative conditions[21] and the effects of environmental injury[22], and ALI-COs could also be used to examine injury or degeneration specifically of axon tracts, such as spinal cord injury, white-matter stroke, or amyotrophic lateral sclerosis. Our hope is that by modelling ever more closely specific features of the developing human brain, one day we will be closer to understanding these debilitating diseases.

Online content

References

1. Lancaster, M. A. et al. Cerebral organoids model human brain development and microcephaly. *Nature* **501**, 373–379 (2013).
2. Kadoshima, T. et al. Self-organization of axial polarity, inside-out layer pattern, and species-specific progenitor dynamics in human ES cell-derived neocortex. *Proc. Natl Acad. Sci. USA* **110**, 20284–20289 (2013).
3. Birey, F. et al. Assembly of functionally integrated human forebrain spheroids. *Nature* **545**, 54–59 (2017).
4. Lancaster, M. A. et al. Guided self-organization and cortical plate formation in human brain organoids. *Nat. Biotechnol.* **35**, 659–666 (2017).
5. Quadrato, G. et al. Cell diversity and network dynamics in photosensitive human brain organoids. *Nature* **545**, 48–53 (2017).
6. Mansour, A. A. et al. An in vivo model of functional and vascularized human brain organoids. *Nat. Biotechnol.* **36**, 432–441 (2018).
7. Gähwiler, B. H., Capogna, M., Debanne, D., McKinney, R. A. & Thompson, S. M. Organotypic slice cultures: a technique has come of age. *Trends Neurosci.* **20**, 471–477 (1997).
8. Renner, M. et al. Self-organized developmental patterning and differentiation in cerebral organoids. *EMBO J.* **36**, 1316–1329 (2017).
9. Bak, M. & Fraser, S. E. Axon fasciculation and differences in midline kinetics between pioneer and follower axons within commissural fascicles. *Development* **130**, 4999–5008 (2003).
10. Polleux, F. & Snider, W. Initiating and growing an axon. *Cold Spring Harb. Perspect. Biol.* **2**, a001925 (2010).
11. Piper, M. et al. Neuropilin 1-Sema signaling regulates crossing of cingulate pioneering axons during development of the corpus callosum. *Cereb. Cortex* **19**(Suppl. 1), i11–i21 (2009).
12. Chédotal, A. & Richards, L. J. Wiring the brain: the biology of neuronal guidance. *Cold Spring Harb. Perspect. Biol.* **2**, a001917 (2010).
13. Shu, T. & Richards, L. J. Cortical axon guidance by the glial wedge during the development of the corpus callosum. *J. Neurosci.* **21**, 2749–2758 (2001).
14. Keeble, T. R. et al. The Wnt receptor Ryk is required for Wnt5a-mediated axon guidance on the contralateral side of the corpus callosum. *J. Neurosci.* **26**, 5840–5848 (2006).
15. Schroeter, M. S., Charlesworth, P., Kitzbichler, M. G., Paulsen, O. & Bullmore, E. T. Emergence of rich-club topology and coordinated dynamics in development of hippocampal functional networks in vitro. *J. Neurosci.* **35**, 5459–5470 (2015).
16. Cotterill, E., Charlesworth, P., Thomas, C. W., Paulsen, O. & Eglen, S. J. A comparison of computational methods for detecting bursts in neuronal spike trains and their application to human stem cell-derived neuronal networks. *J. Neurophysiol.* **116**, 306–321 (2016).
17. Streit, J., Spenger, C. & Lüscher, H. R. An organotypic spinal cord–dorsal root ganglion–]skeletal muscle coculture of embryonic rat. II. functional evidence for the formation of spinal reflex arcs in vitro. *Eur. J. Neurosci.* **3**, 1054–1068 (1991).
18. Koh, T. H. & Eyre, J. A. Maturation of corticospinal tracts assessed by electromagnetic stimulation of the motor cortex. *Arch. Dis. Child.* **63**, 1347–1352 (1988).
19. Daza, R. A. M., Englund, C. & Hevner, R. F. Organotypic slice culture of embryonic brain tissue. *CSH Protoc.* **2007**, t4914 (2007).
20. Sorkin, R. et al. Compact self-wiring in cultured neural networks. *J. Neural Eng.* **3**, 95–101 (2006).
21. Gonzalez, C. et al. Modeling amyloid beta and tau pathology in human cerebral organoids. *Mol. Psychiatry* **23**, 2363–2374 (2018).

22. Qian, X. et al. Brain-region-specific organoids using mini-bioreactors for modeling ZIKV exposure. *Cell* **165**, 1238–1254 (2016).
23. Rezakhaniha, R. et al. Experimental investigation of collagen waviness and orientation in the arterial adventitia using confocal laser scanning microscopy. *Biomech. Model. Mechanobiol.* **11**, 461–473 (2012).

Author contributions

S.L.G. planned and performed experiments, analyzed data, and wrote the manuscript. S.B.M. planned and performed MEA and stimulation experiments, analyzed data and wrote the manuscript. G.M.G. performed the organoid cell dissociation and provided quality control for the single-cell preparation, and L.M.D.W. analyzed the scRNA-seq data. L.M. performed whole-cell electrophysiology experiments and analyzed data under the supervision of M.T. T.S. analyzed MEA electrophysiology data. M.S. generated and maintained organoids and ALI-CO cultures, and analyzed data. J.B. analyzed time-lapse image data. E.D. performed and analyzed time-lapse imaging. O.P. supervised electrophysiology experiments and interpreted data. A.L. planned experiments, analyzed and interpreted data, and supervised G.M.G and L.M.D.W. M.A.L. conceived the project, planned and performed experiments, supervised the project, and wrote the manuscript.

Competing interests

The authors declare no competing interests.

Additional information

Supplementary information is available for this paper at https://doi.org/10.1038/s41593-019-0350-2.

Reprints and permissions information is available at www.nature.com/reprints.

Correspondence and requests for materials should be addressed to M.A.L.

Journal peer review information: *Nature Neuroscience* thanks Alexander Jaworski and other anonymous reviewer(s) for their contribution to the peer review of this work.

Publisher's note: Springer Nature remains neutral with regard to jurisdictional claims in published maps and institutional affiliations.

Methods

Plasmid constructs. The integrating farnesylated GFP construct (pT2-CAG-fGFP, Addgene plasmid #108714) and the sleeping beauty transposase plasmid pCAGEN-SB100X as modified from pCMV-SB100[24] (a gift from Z. Izsvak, Addgene plasmid #34879) were used as previously described[4]. The integrating farnesylated FusionRed (fFusionRed) construct was obtained by replacing EGFP in pT2-CAG-fGFP with FusionRed. pT2-CAG-fGFP was linearized using MluI and EcoRI restriction enzymes. The FusionRed cassette was amplified by PCR from pCi-C-FusionRed-DEST (a gift from H. McMahon) using the following primers: forward 5′-GTGCTGTCTCATCATTTTGGC AAAGAATTCATGGTGAGCGAGCTGATTAAGGAG-3′ and reverse 5′- GAGGGTTCAGCTTACTCACGCGTGATTTACCTCCATCACCAGCGC-3′. The cassette was inserted into the linearized pT2-CAG-farnesyl backbone by Gibson assembly.

Human pluripotent stem cell culture and genome editing. H9 (female) and H1 (male) human embryonic stem cells (obtained from WiCell, and approved for use in this project by the UK Stem Cell Bank Steering Committee) were maintained in StemFlex (Thermo Fisher Scientific, catalogue number A3349401) on Matrigel (Corning, catalogue number 354230) coated plates and passaged twice a week using EDTA. Unless otherwise specified, organoids and ALI-COs shown were generated from H9 cells. For generation of the fFusionRed line the pCAGEN-SB100X (0.125 μg ml⁻¹) plasmid and the transposon donor plasmid pT2-CAG-fFusionRed (0.375 μg ml⁻¹) were transfected into H9 human embryonic stem cells with Lipofectamine Stem (Thermo Fisher Scientific, catalogue number STEM00001). Approximately 10 days after transfection fFusionRed⁺ cells were collected as a pool by fluorescence activated cell sorting on a MoFlo XDP cell sorter (Beckman Coulter).

Generation of cerebral organoids. Cerebral organoids were generated as previously described according to the enCOR method to reliably generate forebrain tissue and a proper cortical plate[4]. In brief, 18,000 cells were plated with PLGA microfilaments prepared from Vicryl sutures. The original set of media described previously[4] or alternatively the STEMdiff Cerebral Organoid Kit (STEMCELL Technologies, catalogue number 08570) were used for organoid culture. From day 35–40 onward the medium was supplemented with 2% dissolved Matrigel basement membrane (Corning, catalogue number 354234) to achieve establishment of the cortical plate. Between days 40 and 60 of the protocol, plasmids were delivered to the organoids by injection and electroporation in the ventricles. Approximately 1–2 weeks after electroporation the organoids were processed for ALI-CO culture.

Electroporation of cerebral organoids. Glass microcapillaries (Drummond Scientific, catalogue number 1–000–0500) were pulled using a P2000 micropipette puller (Suttern Instrument) with the following settings: heat, 550; filament, 5; velocity, 25; delay,150; and pull, 150. The microcapillaries were opened using dissecting scissors to obtain a tip taper of approximately 8–9 mm. A total of 5 μl of a 320 ng μl⁻¹ plasmid solution (80 ng μl⁻¹ pT2-CAG-fGFP and 240 ng μl⁻¹ pCAGEN-SB100) was used for injection and electroporation. Electroporation settings were as previously described[1].

ALI-CO culture. ALI-CO cultures were prepared using a modified slice culture protocol[19]. Mature organoids (approximately 55–60 days old, in some cases up to 90 days) were collected using a cut plastic P1000 pipette tip, washed in HBSS without Ca²⁺ and Mg²⁺ (Thermo Fisher Scientific, catalogue number 14175095) and embedded in 3% low-gelling-temperature agarose (Sigma, catalogue number A9414) at approximately 40 °C in peel-a-way embedding molds (Sigma, catalogue number E6032), typically one to three organoids per mold. The agarose blocks were incubated on ice for 10–15 min and processed on a Leica VT1000S vibrating microtome in cold HBSS. Sections (300 μm thick) were collected onto Millicell-CM cell culture inserts (Millipore, catalogue number PICM0RG50) in six-well plates and left to equilibrate for 1 h at 37 °C in serum-supplemented slice culture medium (SSSCM): DMEM (Invitrogen, catalogue number 10566016), 10% FBS, 0.5% (w/v) glucose, supplemented with penicillin–streptomycin and Fungizone. SSSCM was then replaced with serum-free slice culture medium (SFSCM): Neurobasal (Invitrogen, catalogue number 21103049), 1:50 (v/v) B-27 supplement (Invitrogen, catalogue number 17504044), 0.5% (w/v) glucose, 1× (v/v) Glutamax supplemented with antibiotic–antimycotic (Thermo Fisher Scientific, catalogue number 15240062). ALI-CO cultures were maintained in SFSCM at 37 °C and 5% CO₂ with daily media changes. Media was provided only below the filter insert so that sections stayed at the ALI and were not submerged.

Live imaging and image analysis. For live imaging, ALI-COs were left to flatten for at least one day before extended imaging on a Zeiss LSM 780 or 710 confocal microscope with the incubation chamber set at 7% CO₂ and 37 °C. Time-lapse movies were taken at 10 min intervals over several hours or days. Image analysis was performed in ImageJ. Temporal-projection images were generated from time-lapse stacks using the Temporal-Color Code tool in Fiji. Axon growth-cone tracing was done using MTrackJ[25] with manual tracking of growth cones. Data were then

exported and plotted as the distance from the start of the track over time. Linear regression was performed on all tracks and the average best-fit line calculated for each group (late and early). Orientation analysis of GFP-labeled tracts was done using the OrientationJ analysis plugin[23] using the Gaussian gradient setting, with hue determined by the orientation of tracts, brightness determined by coherency, and saturation set at constant. For quantification of axons in ALI-COs compared with whole organoids, mean gray levels of SMI312 staining were calculated on the entire organoid section of normalized images. For axon-tract morphology measurements of SMI312 staining, OrientationJ was used on Riesz filter setting. Mean gray value was calculated from each of the coherency and energy image outputs, on a region of interest, which was the entire outlined organoid section. These gray values were multiplied to give energy × coherency values. Kymographs were generated using the MultiKymograph tool. For quantification of relative abundance of CTIP2⁺ and CUX2⁺ neurons in whole organoids compared with ALI-COs a total of six whole organoids and six ALI-COs were cryosectioned, stained and imaged. To control for bias and differences in the distribution of neurons in sections of whole organoids or ALI-COs, for each sample two images were acquired, one internal and one near the edge of the tissue. The same approach was taken for the acquisition of the TUNEL assay data. Cell counts were performed in NIS Elements Advanced Research using a quantification macro optimized for each type of quantification separately. Parameter optimization was done on a representative image randomly selected and all images were processed using a batch processing function. TUNEL⁺, CTIP2⁺ and CUX2⁺ cells were defined by the co-expression of DAPI and their respective marker, and their relative abundance was expressed as a ratio to the total number of DAPI⁺ nuclei.

Immunohistochemical analysis. Organoids and ALI-COs were fixed in 4% PFA for 20 min at room temperature or overnight at 4 °C and washed three times in PBS. For cryostat processing, samples were incubated overnight in 30% sucrose. Embedding, cryosectioning and staining were performed as previously described[26] on whole organoids or ALI-COs after removal from the cell-culture insert by cutting the filter around the ALI-CO. For higher magnification staining cryosectioning of ALI-COs was necessary due to their thickness (>300 μm). Whole ALI-COs were stained using a modified protocol. All staining steps were done in permeabilization buffer (0.25% Triton-X, 4% normal donkey serum in PBS) at 4 °C and their duration was extended as follows: permeabilization, overnight; primary and secondary antibody incubation, 2 days; and wash steps (3×), 8 h each. Primary antibodies used with corresponding dilutions were: chicken anti-MAP2 (Abcam, ab5392, 1:50), mouse anti-MAP2 (Chemicon, MAB3418, 1:300), rat anti-CTIP2 (Abcam, ab18465, 1:300), mouse anti-SATB2 (Abcam, ab51502, 1:200), rabbit anti-CUX2 (Abcam ab130395, 1:200), mouse anti-SMI312 (BioLegend, 837904, 1:500), mouse anti-c-Fos (EnCor, MCA-2H2, 1:100), mouse anti-Piccolo (PCLO) (Origene, TA326497, 1:100), mouse anti-STEM121 (Takara, Y40410, 1:500), sheep anti-human-neuropilin-1 (NRP1) (R&D Systems, AF3870, 1:200), rabbit anti-Homer 1 (Synaptic Systems, 160003, 1:100), rabbit anti-Psd95 (Abcam, ab18258, 1:500), mouse anti-human-synaptophysin (EP10) (Thermo Fisher Scientific, 14–6525–80, 1:200), goat anti-human-synaptophysin (R&D Systems, AF5555, 1:100), chicken anti-GFP (Thermo Fisher Scientific, A10262, 1:500), mouse anti-Bassoon (Enzo, SAP7F407, 1:200), rabbit anti-VGAT (Synaptic Systems, 131013, 1:1,000), mouse anti-calretinin (Swant, 63B, 1:500), rat anti-somatostatin (Millipore, MAB354, 1:100), mouse anti-GAD67 (Millipore, MAB5406, 1:100), mouse anti-ephrin-B1 (C-6) (Santa Cruz, sc-515264, 1:50), mouse anti-WNT5A (A-5) (Santa Cruz, sc-365370, 1:50), goat anti-BRN2 (C-20) (Santa Cruz, sc-6029, 1:50), mouse anti-TUBB3 (BioLegend, 801202, 1:500), rabbit anti-RYK (Abcam, ab5518, 1:100), rabbit anti-netrin 1 [EPR5428] (Abcam, ab126729, 1:50), mouse anti-CUX1 (2A10) (Abcam, ab54583, 1:100), rabbit anti-GFAP (Abcam, ab7260, 1:200), rabbit anti-SOX5 (Abcam, ab94396, 1:200). All primary antibodies are well described and validated for immunohistochemistry and were checked for compatibility for human tissue on the basis of similarity to the human sequence. No novel antibodies were generated in this study. Alexa Fluor 405-, 488-, 568- and 647-labeled secondary antibodies (ThermoFisher & Abcam) were used for detection. TdT-mediated dUTP-X nick end labeling (TUNEL) was performed using the In Situ Cell Death Detection Kit TMR red (Sigma, catalogue number 12156792910) as described in the supplier's technical bulletin.

CTB, DiI and emGFP labeling. ALI-COs were visualized on an EVOS FL inverted microscope (Thermo Fisher Scientific) and using a microinjection capillary <0.2 μl of 1 mg ml⁻¹ AlexaFluor 647-conjugated CTB (Thermo Fisher Scientific, catalogue number C34778) or 1–4 DiI crystals (Thermo Fisher Scientific, catalogue number D3911) were applied to the target region. DiI tracing was performed multiple times but owing to difficulty with dye uptake and low signal-to-noise ratio only in one experiment was tracing of sufficient quality for analysis. Similarly, to achieve sparse neuronal labeling, ALI-COs were injected with <0.2 μl of CytoTune emGFP Sendai fluorescence reporter (Thermo Fisher Scientific, catalogue number A16519). Four days after CTB and DiI labeling and 5 days after viral emGFP labeling, the samples were fixed for histological analyses.

Whole-cell patch-clamp recordings. Organoid slices were placed in a submerged chamber and continuously superfused at room temperature with artificial

cerebrospinal fluid containing (in mM): 119 NaCl, 2.5 KCl, 11 glucose, 26 NaHCO$_3$, 1.25 NaH$_2$PO$_4$, 2.5 CaCl$_2$ and 1.3 MgCl$_2$ (pH 7.4), saturated with 5% CO$_2$/95% O$_2$. Whole-cell patch-clamp recordings were performed in current-clamp configuration using an Axon Multiclamp 700B amplifier (Molecular Devices) under a Slicescope (Scientifica) equipped with a ×40 objective lens (Olympus) and a WAT-902H analogue camera (Watec). Signals were filtered at 1 kHz and sampled at 10 kHz with a Digidata 1550 A (Molecular Devices) connected to a computer running pClamp10 (Molecular Devices). Pipettes were pulled from borosilicate glass capillaries (1.5 mm OD × 0.86 mm ID; Harvard Apparatus) and typical pipette resistance was 12–15 MΩ. Pipettes were filled with artificial intracellular solution containing (in mM): 145 K-gluconate, 5 MgCl$_2$, 0.5 EGTA, 2 Na$_2$ATP, 0.2 Na$_2$GTP, 10 HEPES, adjusted to pH 7.2 with KOH (osmolarity: 280–290 mOsm). Resting membrane potential was estimated in current clamp mode immediately after establishing whole cell configuration. Cells with resting membrane potential ≤ −50 mV were selected for analysis (Supplementary Table 1). A series of current steps (800 ms) of increasing amplitude (5 pA increments) were applied in current clamp mode to determine the frequency–current relationship.

Organoid cell dissociation for scRNA-seq. Organoid tissue slices (two slices from an H9 day 53 organoid then cultured under ALI conditions for 22 days; and two slices from each of two H1 day 53 organoids then cultured under ALI conditions for 16 days) were transferred from the ALI into a conical tube (the two slices from the same organoid were pooled) containing Hibernate Medium (Thermo Fisher Scientific, catalogue number A1247601) plus 1× B-27 Supplement (Thermo Fisher Scientific, catalogue number 17504044). Gentle dipping helped remove any remaining agarose. The slices were then placed into a 10 cm^2 tissue culture dish and after washing twice with 1× dPBS (Sigma, catalogue number D8537), transferred into a gentleMACS C Tube (Miltenyi, catalogue number 130–093–237) containing 2 ml of Accumax (Sigma, catalogue number A7089) solution. The C Tube was subsequently attached to the gentleMACS Octo Dissociator (Miltenyi) and ran with the recommended cell dissociation settings. The cell suspension was run through a 70 μm strainer to remove any residual cell and debris clumps. A small volume of the strained cell suspension was removed for cell counts with the remaining being diluted fourfold in 1× dPBS and then centrifuged at 200g for 5 min. The cell pellet was then resuspended in dPBS containing 0.04% BSA (Sigma, catalogue number A9418) to give a final concentration of 206 cells μl^{-1}. This suspension was kept on ice for 30 min until being processed.

scRNA-seq library generation and sequencing. scRNA-seq libraries were prepared as instructed by the manufacturer using the 10X Genomics Chromium Single Cell 3′ Library and Gel Bead Kit (10X Genomics, catalogue number 120237) workflow. The cell suspension (34 μl with a total of 7,000 cells) was loaded onto a 10X Genomics Chromium Single Cell 3′ Chip with the appropriate amount of master mix. The cell capture rate for barcoding varied between 50 and 75%, resulting in 3,500–4,400 barcoded cells. The Chromium Controller was run according to the protocol producing the single-cell gel beads in emulsion mixture. The reverse transcriptase reaction and subsequent amplification was carried out in a C1000 Touch Thermal Cycler (Biorad), with the cDNA being amplified for 12 cycles. Before sequencing, libraries were quality tested using the 2100 Bioanalyzer Instrument (Agilent) and their concentration was measured by quantitative PCR. Samples were pooled together and sequenced on an Illumina Hiseq 4000 platform.

Single-cell data analysis. The scRNA-seq data-analysis pipeline was constructed using the CellRanger, Seurat and Monocle software packages. The reads were aligned to the GRCh38 reference genome using STAR in CellRanger 2.1.1. This provided a gene expression matrix of 13,333 cells with a median of 2,320 genes and 29,086 mean reads per cell post-normalization. Quality of reads (exonic and intronic) were analyzed by FastQC, showing 87.2% fraction reads in cells. Low-quality ends were disregarded during the mapping process. Only reads that were uniquely mapped to the transcriptome were used for unique molecular identifier (UMI) counting in CellRanger. The read depth was normalized in the 'Aggr' function between the libraries of the samples. UMI (transcript) counts were normalized for each cell to the total counts. The values were multiplied by 10,000 and transformed into log-space. Genes expressed in a minimum of three cells and cells expressing between 200 and 5,000 genes with a maximum of 15% mitochondrial genes were opted in during the filtering process. Further data processing was performed using the Seurat v.2.3.0 R package with recommended settings. This yielded a final object of 13,280 cells for the merged libraries, which was then scaled and normalized. Unbiased clustering was achieved by principal component analysis using the highly variable genes that were defined by selecting standard deviation as the dispersion function in the 'FindVariableGenes' option (bin = 20 for the scaled analysis). PCElbowPLot analysis has guided the selection of the maximum number of dimensions assisting the cluster separations process. This was followed by the application of the 'FindClusters' function. Clustering was driven by the recommended resolution of 0.16. Clusters were then visualized in 2D and 3D views based on tSNE separation in R. Robustness of cluster identity was determined comparing top differential genes for each cluster with a cut-off at 25% expression frequency within a population, which identified six well-defined clusters. Cell population identities were determined by gene-enrichment analysis

using cell type, layer, region, dorsoventral position and lobe-specific gene sets obtained from databases (Allen Brain Atlas at http://human.brain-map.org) and published work[1,5,8,27–31]. The final cluster identities were then assigned based on the relative proportion of cells expressing the particular reference genes. GO-term analysis was performed using the Gene Ontology Consortium online software (http://www.geneontology.org). Gene enrichment was defined by Fisher's exact test with FDR multiple test correction, and the top three biological process annotations for the enriched genes were presented on the basis of the highest fold-enrichment amongst the most significant terms ($P < 0.001$). To compare the developmental profile of the organoids and the fetal brain, we used the Monocle R-package to derive a pseudotime trajectory of gene expressions from the scRNA-seq data. The raw gene expression matrix of the 12- and 13-week-old fetal brain[32] were processed through the same quality control and filtering process in Seurat as our organoid derived dataset, which served as input to processing in Monocle. Expression levels across the established pseudotime trajectory were observed for the layer markers and visualized in heat maps comparing data deriving from our organoids and the fetal brain (Supplementary Fig. 5a,b). To compare the representation of distinct developmental cell states in the 69–75-day-old ALI-COs to that seen for three-month-old and 58–65-days-old whole organoids in other studies[5,29], Pearson correlation plots were generated for layer-specific gene expression-profiles obtained from our dataset and published databases (GEO accession codes: GSE86153, GSE75140). For direct comparison the downloaded raw count matrices were uploaded onto Seurat, and filtering was standardized across the datasets. Cells with under 400 genes expressed were discarded, and an upper cap for number of genes analyzed was determined as performed for the analysis of our 69–75-day-old ALI-COs. The analysis was carried out in Python Jupyter and visualized using Python Seaborn (Supplementary Fig. 5c–e).

MEA recordings. ALI-COs used for electrophysiological recordings were kept in BrainPhys (STEMCELL Technologies, catalogue number 05790) supplemented with Neurocult SM1 neuronal supplement (STEMCELL Technologies, catalogue number 05793) for a minimum of 12 h prior to recording. Extracellular recordings of spontaneous activity in the organoid slices ($n = 10$) were made using a MEA system (MEA1600, Multi Channel Systems). Organoid slices were transferred immediately before recording to a 3D grid MEA (Multi Channel Systems, 60–3DMEA200/12iR-Ti-gr, 60 electrodes, 12 μm diameter, 200 μm spacing, with an internal reference electrode). Media was removed until a thin layer remained allowing the slice to settle on the 3D MEA grid. The temperature was maintained at 37 °C (TC01 controller and TCX-Control software, Multi Channel Systems). During some recordings, tetrodotoxin (1–2 μM in warm media) was applied to the slice using a Pasteur pipette, which was sufficient to block activity ($n = 3$). The signal was sampled at 25 kHz and stored using the 64-channel data acquisition board (MC Card) and MC Rack software (both Multi Channel Systems). Any electrodes with noise fluctuations greater than 50 μV were grounded before recording. Data were exported as a binary file to Matlab (MathWorks) for analysis. The raw signal was bandpass filtered (third-order Butterworth, 600–8,000 Hz) and a threshold six times the standard deviation above the background noise was used to detect extracellular spike waveforms in each channel with a 2 ms refractory period imposed after each detected spike. Correlated spontaneous activity was compared between electrodes using the spike-time tiling coefficient[33] with a synchronicity window (Δt) of 40 ms by translating the publicly available code in C (https://github.com/CCutts/Detecting_pairwise_correlations_in_spike_trains) to Matlab.

Mouse spinal cord–ALI-CO co-culture. For mouse embryo spinal cord dissection, C57BL/6 wild-type pregnant female mice (12.5 days after conception) were killed and uterine horns collected. Mouse tissue was collected in accordance with the UK Animals (Scientific Procedures) Act 1986 and European Community Council Directive on Animal Care by a trained technician of the MRC-LMB animal facilities. All steps described from this point on were carried out in ice-cold PBS without Ca^{2+} and Mg^{2+}. The uterine horns were cut between implantation sites to separate the embryos. Using precision tweezers (IDEAL-TEK, catalogue number 5SA) the muscle layer, the decidua and remaining extra-embryonic tissue were removed to isolate individual embryos (E12.5). For isolation of spinal cords together with dorsal root ganglia and paraspinal muscles, 0.15 mm diameter dissecting pins (Fine Science Tools, catalogue number 2600215) were inserted in the head and pelvic-regions to stabilise the embryo. First, the embryo was placed ventral side down, the dorsal epithelium was removed and the embryo was cut along its length in a posterior-to-anterior fasion, at a distance of approximately 1 mm from the midline, on either side of the spinal cord, using 3 mm cutting edge spring scissors (CohanVannas, catalogue number 15000–01). The embryo was then repositioned on its side and internal organs removed. Lastly, the embryo was placed ventral side up, any remaining undesired tissue was removed including the head and tail.

The dissected mouse spinal cords with surrounding muscle tissue were incubated in ice-cold PBS until embedding. Typically, one organoid and two mouse tissues were first washed in ice-cold HBSS without Ca^{2+} and Mg^{2+}, then washed and embedded in 3% low-gelling-temperature agarose at approximately 40 °C. Before sectioning and before agarose polymerization, the organoid was positioned centrally at the bottom of the mold on top of a layer of solidified agarose. The

mouse tissues were placed flat on either side with their roof plates facing inwards towards the organoid (approximately 1–3 mm away). The organoid was oriented such that its longest axis would be parallel to the spinal cords, thus ensuring the maximum number of slices cut that included both organoid and mouse tissue. The block was oriented on the stage for sectioning along the axial plane of the spinal cords. Sectioning was performed as outlined above. Mouse–organoid co-culture slices were maintained on SFSC medium with daily media changes. After 2–3 weeks human tracts could be seen innervating mouse spinal cords.

ALI-CO stimulation and axotomy. Spontaneous contractions of mouse spinal muscles in the organoid–mouse co-cultures were typically observed after 20–30 days in co-culture using light microscopy and were recorded using a Nikon TE2000 equipped with Andor Neo sCMOS camera using the NIS Elements software for image acquisition. Images were acquired at approximately 2.3 Hz or 60 Hz for estimation of latency. Data were acquired as either an '.avi' or '.nd2' file and analyzed using a custom macro in ImageJ (NIH) to calculate the displacement of the tissue on muscle contraction as a function of time. Muscle contractions evoked by extracellular stimulation of the organoid axonal tracts were elicited using a stainless steel electrode (A-M Systems, catalogue number 57100) connected to a constant-current isolated stimulator (0.2–30 mA, 120–180 μs manually- or transistor-to-transistor logic (TTL)-triggered pulses, model DS3, Digitimer). When operating the stimulator in TTL-triggered mode, TTL pulses of a given frequency (5 ms duration) were generated using an Arduino running on its internal clock.

For analyses of the latency, we simultaneously recorded the TTL triggers (which trigger the stimulator) and the camera 'expose-out' TTL (which indicates when each frame is exposed) using an oscilloscope with a sampling rate of 200 kHz (Picoscope 2406B). This allowed us to precisely (± 5 μs) measure the delay between the first frame of the movie and the previous TTL pulse, from which we could compute the time delay between each frame and the previous stimulation based on the hardware timestamps of each frame and the frequency of the TTL pulses.

Application of TTX (2 μM) abolished muscle contractions evoked by axon-tract stimulation after 15 min ($n = 2$). Washing the co-culture with warm media to remove the TTX restored the ability to evoke muscle contractions after 30 min in the incubator at 37 °C in one of the experiments. For axotomy, the filters were retrieved from the imaging vessels, placed on a plastic support, visualized on an inverted cell culture microscope at ×10 magnification and the incision was performed using a microknife (FST, catalogue number 10316–14). To detect the muscle activity from acquired image sequences, the average of the difference between two consecutive frames for the region of interest was computed. The resulting temporal signal was then decomposed into the sum of a baseline, stimulation and residual motion. The baseline was estimated as a 1D rolling ball and the stimulation peaks were detected as outliers (12 × s.d.) from the mean. The overall processing was implemented as a macro for ImageJ that was applied to a selected region of interest. The fire TTL signal was used to synchronize the acquired images and the electrical stimulation signal, the latencies were computed using a Matlab script as the delay between each recorded stimulation TTL pulse and the time when the nearest residual motion went above 2 × s.d.

Statistics. Statistical comparisons performed as stated in figure legends included Mann–Whitney unpaired two-tailed test, Fisher's exact test with FDR multiple test correction (FDR > 0.001), Pearson correlation of layer-specific gene expression, and correlation of neural activity determined using the spike-time tiling coefficient

as detailed above. No statistical methods were used to pre-determine sample sizes owing to the exploratory nature of the experiments, but our sample sizes are similar to those reported in previous publications[4,8]. In cases of different treatments (ALI-CO versus whole) organoid samples were randomly assigned to the two treatments by taking organoids from within the same culture vessels and randomly separating into whole-organoid or ALI-culture conditions. Because of the nature of the treatments being obviously different in terms of culture paradigm, data collection and analysis were not performed blind to the conditions of the experiments.

Reporting summary. Further information on research design is available in the Nature Research Reporting Summary linked to this article.

Code availability

All custom code for the MEA analysis in this paper is publicly available at https://github.com/Timothysit/organoids. The code used for latency analysis can be accessed at the following link: https://github.com/jboulanger/stimulation-motion.

Data availability

The data that support the findings of this study are included in the Supplementary Information with the paper. All scRNA-seq data has been deposited on GEO, accession number GSE124174. Raw data (for example, raw images and electrophysiological recordings) is available upon request from the corresponding author.

References

24. Mátés, L. et al. Molecular evolution of a novel hyperactive Sleeping Beauty transposase enables robust stable gene transfer in vertebrates. *Nat. Genet.* **41**, 753–761 (2009).
25. Meijering, E., Dzyubachyk, O. & Smal, I. Methods for cell and particle tracking. *Meth. Enzymol.* **504**, 183–200 (2012).
26. Lancaster, M. A. & Knoblich, J. A. Generation of cerebral organoids from human pluripotent stem cells. *Nat. Protoc.* **9**, 2329–2340 (2014).
27. Zhong, S. et al. A single-cell RNA-seq survey of the developmental landscape of the human prefrontal cortex. *Nature* **555**, 524–528 (2018).
28. Watanabe, M. et al. Self-organized cerebral organoids with human-specific features predict effective drugs to combat Zika virus infection. *Cell Rep.* **21**, 517–532 (2017).
29. Pollen, A. A. et al. Molecular identity of human outer radial glia during cortical development. *Cell* **163**, 55–67 (2015).
30. Preissl, S. et al. Single-nucleus analysis of accessible chromatin in developing mouse forebrain reveals cell-type-specific transcriptional regulation. *Nat. Neurosci.* **21**, 432–439 (2018).
31. Lake, B. B. et al. Neuronal subtypes and diversity revealed by single-nucleus RNA sequencing of the human brain. *Science* **352**, 1586–1590 (2016).
32. Camp, J. G. et al. Human cerebral organoids recapitulate gene expression programs of fetal neocortex development. *Proc. Natl Acad. Sci. USA* **112**, 15672–15677 (2015).
33. Cutts, C. S. & Eglen, S. J. Detecting pairwise correlations in spike trains: an objective comparison of methods and application to the study of retinal waves. *J. Neurosci.* **34**, 14288–14303 (2014).

nature research

Corresponding author(s):	Madeline Lancaster
Last updated by author(s):	Jan 1, 2019

Reporting Summary

Nature Research wishes to improve the reproducibility of the work that we publish. This form provides structure for consistency and transparency in reporting. For further information on Nature Research policies, see Authors & Referees and the Editorial Policy Checklist.

Statistics

For all statistical analyses, confirm that the following items are present in the figure legend, table legend, main text, or Methods section.

n/a	Confirmed	
☐	☒	The exact sample size (n) for each experimental group/condition, given as a discrete number and unit of measurement
☐	☒	A statement on whether measurements were taken from distinct samples or whether the same sample was measured repeatedly
☐	☒	The statistical test(s) used AND whether they are one- or two-sided *Only common tests should be described solely by name; describe more complex techniques in the Methods section.*
☐	☒	A description of all covariates tested
☐	☒	A description of any assumptions or corrections, such as tests of normality and adjustment for multiple comparisons
☐	☒	A full description of the statistical parameters including central tendency (e.g. means) or other basic estimates (e.g. regression coefficient) AND variation (e.g. standard deviation) or associated estimates of uncertainty (e.g. confidence intervals)
☐	☒	For null hypothesis testing, the test statistic (e.g. F, t, r) with confidence intervals, effect sizes, degrees of freedom and P value noted *Give P values as exact values whenever suitable.*
☒	☐	For Bayesian analysis, information on the choice of priors and Markov chain Monte Carlo settings
☒	☐	For hierarchical and complex designs, identification of the appropriate level for tests and full reporting of outcomes
☒	☐	Estimates of effect sizes (e.g. Cohen's d, Pearson's r), indicating how they were calculated

Our web collection on statistics for biologists contains articles on many of the points above.

Software and code

Policy information about availability of computer code

Data collection	Nikon NIS Elements software; Zeiss Zen acquisition software; pClamp10 software, Molecular Devices; TCX-Control software, MC Rack software, Multi Channel Systems; Illumina Hiseq 4000 platform
Data analysis	ImageJ, MultiKymograph, MTrackJ, FIJI Temporal Color Code, R, Matlab (MathWorks), Custom Matlab script described in methods and available at https://github.com/jboulanger/stimulation-motion, NIS Elements Advanced Research with custom macro available on request, code for MEA analysis available at https://github.com/Timothysit/organoids; STAR in CellRanger 2.1.1, Seurat 2.3.0 R package, Monocle R-package; Gene Ontology Consortium online software (http://www.geneontology.org); Python Jupyter and Python Seaborn.

For manuscripts utilizing custom algorithms or software that are central to the research but not yet described in published literature, software must be made available to editors/reviewers. We strongly encourage code deposition in a community repository (e.g. GitHub). See the Nature Research guidelines for submitting code & software for further information.

Data

Policy information about availability of data

All manuscripts must include a data availability statement. This statement should provide the following information, where applicable:

- Accession codes, unique identifiers, or web links for publicly available datasets
- A list of figures that have associated raw data
- A description of any restrictions on data availability

The data that support the findings of this study are included in the supporting material with the paper. scRNA-seq data have been deposited on GEO, accession number GSE124174. Raw data (e.g. raw images and electrophysiological recordings) is available upon request from the corresponding author.

Field-specific reporting

Please select the one below that is the best fit for your research. If you are not sure, read the appropriate sections before making your selection.

☒ Life sciences　　　☐ Behavioural & social sciences　　　☐ Ecological, evolutionary & environmental sciences

For a reference copy of the document with all sections, see nature.com/documents/nr-reporting-summary-flat.pdf

Life sciences study design

All studies must disclose on these points even when the disclosure is negative.

Sample size	Because of the exploratory nature of the study, sample size was the most available samples available. Statistical comparisons were done on as many samples as were available.
Data exclusions	No data or samples were excluded.
Replication	Multiple samples at various times were analyzed by independent approaches (ie. histologic, molecular analysis, functional analysis) and all experiments were performed more than once. DiI tracing was performed multiple times but due to difficulty with dye take-up only one experiment showed substantial tracing, which is included in the figure. TTX abolition of muscle contractions was performed twice, both of which abolished contractions, but only once were contractions reacquired after wash-out.
Randomization	There were no statistical comparisons between different groups that required randomization.
Blinding	For counting retrograde labeling neuronal identity, the scientist who collected images coded the file names and a second scientist counted cell identities.

Reporting for specific materials, systems and methods

We require information from authors about some types of materials, experimental systems and methods used in many studies. Here, indicate whether each material, system or method listed is relevant to your study. If you are not sure if a list item applies to your research, read the appropriate section before selecting a response.

Materials & experimental systems

n/a	Involved in the study
☐	☒ Antibodies
☐	☒ Eukaryotic cell lines
☒	☐ Palaeontology
☒	☐ Animals and other organisms
☒	☐ Human research participants
☒	☐ Clinical data

Methods

n/a	Involved in the study
☒	☐ ChIP-seq
☒	☐ Flow cytometry
☒	☐ MRI-based neuroimaging

Antibodies

Antibodies used	Primary antibodies used with corresponding dilutions were: chicken anti-MAP2 (Abcam, ab5392, 1:500), mouse anti-MAP2 (Chemicon, MAB3418, 1:300), rat anti-CTIP2 (Abcam, ab18465, 1:300), mouse anti-SATB2 (Abcam, ab51502, 1:200), rabbit anti-CUX2 (Abcam ab130395, 1:200), mouse anti-SMI312 (BioLegend, 837904, 1:500), mouse anti-c-Fos (EnCor, MCA-2H2, 1:100), mouse anti-Piccolo (PCLO) (Origene, TA326497, 1:100), mouse anti-STEM121 (Takara, Y40410, 1:500), sheep anti-human-Neuropilin-1 (NRP1) (R&D Systems, AF3870, 1:200), rabbit anti-Homer 1 (Synapti Systems, 160003, 1:100), rabbit anti-PSD95 (Abcam, ab18258, 1:500), mouse anti-human-Synaptophysin (EP10) (ThermoFisher, 14-6525-80, 1:200), goat anti-human-Synaptophysin (R&D Systems, AF5555, 1:100), chicken anti-GFP (ThermoFisher, A10262, 1:500), mouse anti-Bassoon (Enzo, SAP7F407, 1:200), rabbit anti-VGAT (Synaptic Systems, 131013, 1:1000), mouse anti-Calretinin (Swant, 63B, 1:500), rat anti-Somatostatin (Millipore, MAB354, 1:100), mouse anti-GAD67 (Millipore, MAB5406, 1:100), mouse anti-Ephrin-B1 (C-6) (Santa Cruz, sc-515264), mouse anti-WNT5A (A-5) (Santa Cruz, sc-365370), goat anti-BRN2 (C-20) (Santa Cruz, sc-6029), mouse anti-TUBB3 (BioLegend, #801202), rabbit anti-RYK (Abcam, ab5518), rabbit anti-Netrin 1 [EPR5428] (Abcam, ab126729), mouse anti-CUX1 [2A10] (Abcam, ab54583), rabbit anti-GFAP (Abcam, ab7260), rabbit anti-SOX5 (Abcam, ab94396).
Validation	All antibodies used were well-described and tested in the literature. No antibodies were novel antibodies not previously validated in the literature or according to the manufacture. All antibodies were checked for reactivity to the human variant to be sure of compatibility with staining in human organoid tissue.

Eukaryotic cell lines

Policy information about cell lines

Cell line source(s)	Human embryonic stem cells (H9 and H1)
Authentication	Cells were authenticated by CNV analysis.
Mycoplasma contamination	Mycoplasma testing was done routinely every month and all cell lines tested negative.
Commonly misidentified lines (See ICLAC register)	No commonly misidentified cell lines were used.